Research Square

Preprints are preliminary reports that have not undergone peer review.
They should not be considered conclusive, used to inform clinical practice,
or referenced by the media as validated information.

Droplet Spreading on Nanowall-Textured Hydrophobic Surfaces: A Nonlinear Reduced-Order Model

Mubarak Yakubu

mubarak.yakubu@ku.ac.ae

Khalifa University of Science and Technology https://orcid.org/0000-0002-9403-6770

Najib Aminu Ismail

naismail@abu.edu.ng

Ahmadu Bello University

Research Article

Keywords: Droplet impact, maximum spreading, reduced-order model, nanowall texture, hybrid dynamics, hydrophobic surfaces

Posted Date: October 5th, 2026

DOI: https://doi.org/10.21203/rs.3.rs-11221595/v1

License: This work is licensed under a Creative Commons Attribution 4.0 International License.
Read Full License

Additional Declarations: The authors declare no competing interests.

Droplet Spreading on Nanowall-Textured Hydrophobic Surfaces: A Nonlinear Reduced-Order Model

Najib Aminu Ismail[1] and Mubarak Yakubu[2]

[1]Department of Mechanical Engineering, Ahmadu Bello University, Zaria, Kaduna, Nigeria
[2]Khalifa University, Abu Dhabi 127788, United Arab Emirates

September 30, 2026

Abstract

A nonlinear one-degree-of-freedom model is formulated for the effective radial deformation of water droplets impacting smooth and nanowall-textured hydrophobic silicon surfaces. The model is a lumped radial surrogate, not a resolved volume-of-fluid, phase-field, or other multiphase simulation. Capillary stiffness is fixed by an inertial–capillary timescale, a cubic stiffness is calibrated to one graphically extracted smooth-surface spread factor, and the nanowall contribution is represented by regularized kinetic resistance together with an explicit moving-to-stuck event. For a 20 μL droplet released from 20 mm, the linear unpinned oscillator gives a maximum spread factor of 3.955, the calibrated nonlinear unpinned oscillator gives 2.253, and the nonlinear textured-surface model gives 1.810. With the parameters fixed, the predicted maximum spread increases with reconstructed Weber number and remains lower for the textured surface over the investigated volume and release-height conditions, consistent with the qualitative trends reported by Yilbas et al. Pointwise experimental errors are not claimed because numerical response data were not available. Local deterministic sensitivity identifies nonlinear stiffness and pinning magnitude as the principal controls on maximum spread; solver refinement, event-root tolerance, and the kinetic-force smoothing speed have negligible effects at the reported precision. The model does not predict physical lift-off, vertical rebound, wetting-state transitions, or the experimental normal restitution coefficient.

Keywords: droplet impact; maximum spreading; reduced-order model; nanowall texture; hybrid dynamics; hydrophobic surfaces

1 Introduction

Droplet impact on a non-wetting solid is a transient conversion among translational kinetic energy, interfacial energy, internal liquid motion, and dissipation. During the initial spreading stage, inertia enlarges the wetted or projected footprint while capillarity increasingly resists deformation. Viscous stresses in the bulk and lamella, together with moving-contact-line losses, reduce the energy available for subsequent retraction. The relative importance of these processes is commonly organized by the Weber, Reynolds, and Ohnesorge numbers. For low-viscosity droplets on sufficiently non-wetting surfaces, the classical capillary–inertial result $\beta_{\max} \sim We^{1/4}$ captures an important leading-order trend, whereas viscous corrections become increasingly important as the liquid or near-wall dissipation increases [1, 2]. Such scaling laws are valuable summaries of the maximum deformation, but they do not uniquely identify how a textured surface modifies the underlying force and energy balances.

Surface texture introduces at least three conceptually distinct effects. First, it changes the equilibrium wetting geometry: idealized Wenzel and Cassie–Baxter descriptions associate roughness with fully impregnated and composite solid–liquid–gas configurations, respectively [3, 4]. Second, edges and chemical or geometric heterogeneities create energy barriers that can arrest or intermittently release the three-phase contact line. The resulting response depends on advancing and receding states and cannot generally be inferred from one apparent static contact angle [5, 6]. Third, an impacting liquid may penetrate a texture, displace or compress gas, and alter both dissipation and recoverable interfacial or gas energy. Transitions between suspended and penetrated configurations can consequently change spreading, recoil, and rebound in different ways [7, 8]. A smaller maximum footprint may therefore reflect enhanced capillary resistance, contact-line pinning, additional dissipation, altered wetting geometry, or some combination of these mechanisms.

This distinction matters because maximum spread and rebound are not interchangeable measures of impact dynamics. Maximum spread is primarily an in-plane deformation observable, reached when the outward radial motion first vanishes. Rebound height or the normal restitution coefficient instead depends on the later conversion of stored energy into vertical center-of-mass motion. A surface can restrict radial spreading yet still return energy efficiently in the normal direction, provided that the relevant storage and momentum-redirection mechanisms are present. Conversely, a contact line can reach a small maximum radius because energy has been irreversibly dissipated, in which case strong rebound would not follow. Studies of droplets in inclined V-shaped hydrophobic channels further show that unequal wetting and pinning on opposing walls can generate coupled translation, rolling, and spinning, including rotational motion used to enlarge dust-cleaning paths [9, 10]. These asymmetric modes reinforce why a model that represents texture only through radial resistance must not interpret its maximum-spread prediction as a prediction of vertical rebound or general three-dimensional droplet motion.

The experiments of Yilbas et al. [11] provide the specific setting considered here. They examined water droplets impacting hydrophobized smooth and nanowall-textured silicon. The nanowall surface had a reported average spacing of 130 nm, a height of 10.45 μm, an apparent contact angle of $158^\circ \pm 2^\circ$, and a contact-angle hysteresis of $4^\circ \pm 1^\circ$. Relative to the hydrophobized smooth wafer, the textured surface produced a smaller maximum spreading diameter over the investigated droplet volumes and release heights. The same study also reported rebound behavior and discussed penetration-induced trapped-air pressurization. Related impact experiments on hydrophobized PDMS micro-post arrays connected texture spacing and spreading dynamics to the area cleaned by an impacting droplet, illustrating the practical relevance of maximum footprint to environmental dust mitigation [12]. These observations point to competing texture effects: contact-line resistance can limit the outward footprint, while texture-scale liquid–gas dynamics may influence later normal recovery. The available spread plots constrain the radial response, but they do not by themselves separate pinning, viscous loss, nonlinear deformation stiffness, and recoverable texture energy.

Reduced-order oscillators offer a way to ask a deliberately narrower question: what is the simplest radial dynamical system that reproduces the observed direction and condition dependence of maximum spreading? Capillary–inertial oscillator analogies have long been used to organize droplet deformation and oscillation timescales [13, 14]. A linear oscillator, however, assigns an amplitude-independent restoring stiffness and can become unrealistically compliant at the large deformations reached during impact. Adding nonlinear stiffness provides an aggregate representation of deformation modes omitted from a single coordinate. Likewise, a direction-opposing force can represent the work required to move a contact line across texture, but a smooth regularization of Coulomb-like resistance vanishes at zero velocity and cannot, without a separate rule, sustain static pinning. These observations motivate both the cubic restoring term and the explicit hybrid moving/stuck structure used below.

The reduced description also exposes an identifiability limitation. A measured value of $\beta_{\max}$ supplies one scalar constraint, while nonlinear stiffness, viscous damping, and pinning resistance can all reduce the predicted amplitude. Agreement at one condition therefore cannot validate each closure separately. A defensible reduced-order study must distinguish fitted, derived, and assumed quantities; demonstrate which term corrects which model deficiency; transfer fixed parameters to other conditions; and report sensitivity to both physical closures and numerical event definitions. This is the role of the model hierarchy and deterministic sensitivity analysis in the present work.

Resolved interface simulations can, in principle, represent pressure, interface shape, gas entrapment, dynamic contact angles, and changes of wetting state when supplied with adequate spatial resolution and constitutive boundary models [6, 8]. Directly resolving a millimetric droplet together with a texture whose characteristic spacing is 130 nm spans more than four orders of magnitude in length before additional interface and contact-line refinement is considered. The present model is not a replacement for that description. It is a computationally inexpensive radial surrogate intended to define what can and cannot be inferred from the available maximum-spread information.

Accordingly, this work develops a nonlinear one-degree-of-freedom model with: (i) a consistently defined effective radial coordinate and explicit lumped mass and velocity-projection assumptions; (ii) capillary stiffness fixed by the inertial–capillary timescale and one cubic coefficient calibrated to a smooth-surface spread value; (iii) a fixed-reference nanowall resistance closure combined with a mathematically stated moving-to-stuck event; and (iv) model-hierarchy, cross-condition, local-sensitivity, and numerical-refinement tests. The supported claims concern maximum-spread trends and the behavior of this surrogate. No resolved multiphase field, wetting-state transition, physical contact time, lift-off event, or vertical rebound prediction is presented.

2 Reduced-Order Formulation

2.1 Effective radial coordinate and moving dynamics

Let $q(t)$ denote an *effective radial extent*, with reference value

$$q_0 = \frac{D_0}{2}, \tag{1}$$

where D_0 is the equivalent spherical diameter of the incident droplet. The effective diameter is $D_{\mathrm{eff}}(t) = 2q(t)$ and the maximum spread factor is

$$\beta_{\max} = \frac{D_{\mathrm{eff,max}}}{D_0} = \frac{q_{\max}}{q_0}. \tag{2}$$

The coordinate is not identified with the physical wetted contact-line radius at the instant of first contact. Instead, $q(0) = q_0$ defines the undeformed reference size from which the lumped radial deformation is measured. This interpretation removes the inconsistency that would arise from calling $D_0/2$ an initial physical contact radius.

While the model is in its moving state, the coordinate satisfies

$$m\ddot{q} = -k_{\mathrm{cap}}(q - q_0)\left[1 + \kappa_s\left(\frac{q - q_0}{q_0}\right)^2\right] - c_{\mathrm{visc}}\dot{q} - F_{\mathrm{pin}}\tanh\left(\frac{\dot{q}}{v_s}\right). \tag{3}$$

The effective mass is set equal to the droplet mass,

$$m = \rho\frac{\pi D_0^3}{6}, \tag{4}$$

and the initial conditions are

$$q(0) = q_0, \qquad \dot{q}(0) = v_i. \tag{5}$$

Using the complete droplet mass and mapping the incident speed v_i directly to the initial generalized speed are lumped projection assumptions. They make the initial generalized kinetic energy equal to the incident translational kinetic energy, but they are not derived from a resolved impact velocity field.

The capillary stiffness is

$$k_{\mathrm{cap}} = \frac{4\pi}{3}\gamma. \tag{6}$$

Consequently, the linear natural timescale equals

$$\sqrt{\frac{m}{k_{\mathrm{cap}}}} = \sqrt{\frac{\rho D_0^3}{8\gamma}} \equiv \tau_c. \tag{7}$$

Thus k_{cap} is derived from the selected inertial–capillary timescale rather than fitted. The dimensionless cubic coefficient κ_s supplies amplitude-dependent stiffening. The damping coefficient is written

$$c_{\mathrm{visc}} = 2\zeta\sqrt{k_{\mathrm{cap}} m}, \qquad \zeta = \frac{\zeta_0(1+\phi)}{\sqrt{Re}}, \tag{8}$$

where $\phi = 0$ for the smooth surface and $\phi = 0.30$ for the textured calculation. The dimensionless prefactor ζ_0 is an assumed closure parameter.

The last term of Equation (3) is a regularized, direction-opposing kinetic resistance. Its magnitude approaches F_{pin} when $|\dot{q}| \gg v_s$. Because the term is zero at $\dot{q} = 0$, it cannot maintain a statically pinned state against a nonzero capillary force. Static pinning is therefore handled separately.

2.2 Hybrid static-pinning rule

Define the magnitude of the capillary driving force as

$$F_{\mathrm{cap}}(q) = k_{\mathrm{cap}}|q - q_0| \left[1 + \kappa_s \left(\frac{q - q_0}{q_0}\right)^2\right]. \tag{9}$$

The moving-to-stuck time is imposed as

$$t_s = \inf\left\{t > 0 : |\dot{q}(t)| \le v_{\mathrm{stick}} \text{ and } F_{\mathrm{cap}}(q(t)) \le \eta_s F_{\mathrm{pin}}\right\}, \tag{10}$$

where v_{stick} is a numerical capture band and η_s is a dimensionless static-capacity factor. If this condition is reached before radial return, the reported moving trajectory terminates at t_s. A formal stuck continuation would have

$$q(t) = q(t_s), \qquad \dot{q}(t) = 0, \qquad t \ge t_s, \tag{11}$$

with the static reaction taking whatever value is required up to $\eta_s F_{\mathrm{pin}}$. Such a continuation is not plotted because the model contains no physical detachment or depinning rule. Equation (10) is a hybrid modeling rule, not a consequence of the regularized kinetic term and not an experimentally validated contact-line law.

2.3 Fixed-reference pinning closure

The pinning magnitude is estimated from a pore-scale force used by Yilbas et al. [11],

$$F_{\text{site}} = \pi D_H \gamma |\cos\theta^*|, \tag{12}$$

combined with a fixed reference-radius encounter count

$$n_0 = \frac{\pi q_0}{a}, \qquad F_{\text{pin}} = n_0 F_{\text{site}}. \tag{13}$$

Here $2a = 130$ nm is the reported mean spacing, $heta^* = 158^\circ$ is the reported apparent contact angle, and the hydraulic diameter is assumed to be $D_H = 2a$. The count n_0 is fixed at the reference radius; it does not grow with $q(t)$. It is therefore a reduced-order scale approximation rather than a literal count of all texture cells contacted by a moving contact line.

With $D_H = 2a$, the spacing cancels:

$$F_{\text{pin}} = 2\pi^2 q_0 \gamma |\cos\theta^*|, \qquad \Pi_{\text{pin}} \equiv \frac{F_{\text{pin}}}{k_{\text{cap}} q_0} = \frac{3\pi}{2} |\cos\theta^*|. \tag{14}$$

This cancellation makes the selected dimensionless pinning magnitude independent of both the assumed spacing and droplet size. It is a direct consequence of combining $D_H = 2a$ with $n_0 \propto q_0/a$, and it limits the closure's ability to distinguish textures of different spacing. The closure is used transparently as a scenario estimate; it is not claimed to have been independently validated.

2.4 Dimensionless form and moving-state energy

With $x = (q - q_0)/q_0$ and $s = t/\tau_c$, Equation (3) becomes

$$x'' = -x(1 + \kappa_s x^2) - 2\zeta x' - \Pi_{\text{pin}} \tanh\left(\frac{x'}{\varepsilon}\right), \tag{15}$$

where primes denote differentiation with respect to s and

$$\varepsilon = \frac{v_s \tau_c}{q_0}. \tag{16}$$

The static rule is equivalently $|x'| \le v_{\text{stick}} \tau_c / q_0$ and $|x(1 + \kappa_s x^2)| \le \eta_s \Pi_{\text{pin}}$.

During a moving interval, define

$$E = \frac{1}{2} m \dot{q}^2 + \frac{1}{2} k_{\text{cap}} (q - q_0)^2 + \frac{k_{\text{cap}} \kappa_s}{4 q_0^2} (q - q_0)^4. \tag{17}$$

Along a solution of Equation (3),

$$\frac{dE}{dt} = -c_{\text{visc}} \dot{q}^2 - F_{\text{pin}} \dot{q} \tanh(\dot{q}/v_s) \le 0. \tag{18}$$

Equation (18) shows that the viscous and regularized pinning terms dissipate generalized mechanical energy along a given moving trajectory. It does not, by itself, establish every possible ordering between trajectories with different parameters or different hybrid switching times.

3 Parameters and Numerical Method

3.1 Reconstructed impact conditions

Water properties are set to $\rho = 998\ \mathrm{kg\,m^{-3}}$, $\mu = 1.00 \times 10^{-3}\ \mathrm{Pa\,s}$, and $\gamma = 0.072\ \mathrm{N\,m^{-1}}$. For a nominal volume V and release height h, the spherical-equivalent diameter and ballistic impact speed are reconstructed as

$$D_0 = \left(\frac{6V}{\pi}\right)^{1/3}, \qquad v_i = \sqrt{2gh}. \tag{19}$$

The second expression neglects aerodynamic drag and any release-system effects; v_i is therefore reconstructed rather than directly measured. The dimensionless groups are

$$We = \frac{\rho v_i^2 D_0}{\gamma}, \qquad Re = \frac{\rho v_i D_0}{\mu}, \qquad Oh = \frac{\mu}{\sqrt{\rho\gamma D_0}} = \frac{\sqrt{We}}{Re}. \tag{20}$$

For $V = 20\ \mu\mathrm{L}$ and $h = 20$ mm, these relations give $D_0 = 3.368$ mm, $v_i = 0.626\ \mathrm{m\,s^{-1}}$, $We = 18.32$, $Re = 2.105 \times 10^3$, $Oh = 2.033 \times 10^{-3}$, and $\tau_c = 8.135$ ms.

3.2 Parameter classification

Table 1 separates source quantities, reconstructed and analytical quantities, the fitted coefficient, closure assumptions, and numerical event parameters. This classification is important because the model is not fully determined by independently measured material constants.

Table 1: Base-case quantities and their status. Values apply to $V = 20\ \mu\mathrm{L}$ and $h = 20$ mm unless stated otherwise.

Category	Quantity	Value	Status or source
Literature/property	ρ, μ, γ	998, 10^{-3}, 0.072 SI	Water-property values used in the calculation
Literature/property	$2a$, θ^*, ϕ	130 nm, 158°, 0.30	Texture/contact-angle inputs from Ref. [11]
Reconstructed	D_0, v_i	3.368 mm, $0.626\ \mathrm{m\,s^{-1}}$	Equation (19)
Derived	We, Re, Oh, τ_c	18.32, 2105, 2.033×10^{-3}, 8.135 ms	Equations (7) and (20)
Derived	m, k_{cap}	1.996×10^{-5} kg, $0.3016\ \mathrm{N\,m^{-1}}$	Lumped mass and Equation (6)
Fitted	κ_s	6.0	One smooth-surface graphical target; Section 3.3
Assumed closure	ζ_0	0.70	Damping prefactor; sensitivity checked
Assumed closure	D_H, n_0	$2a$, $\pi q_0/a$	Fixed-reference pinning approximation
Assumed closure	F_{pin}, Π_{pin}	2.22×10^{-3} N, 4.369	Consequences of Equation (14)
Assumed closure	v_s	$10^{-4}\ \mathrm{m\,s^{-1}}$	Kinetic-force regularization speed
Numerical event	v_{stick}, η_s	$10^{-3}\ \mathrm{m\,s^{-1}}$, 1.0	Moving-to-stuck rule
Numerical solver	rtol, atol, $\Delta t_{\max}$	10^{-6}, 10^{-10}, $\tau_c/25$	Baseline RK45 settings
Numerical event	root tolerance	10^{-10} s	Event localization

3.3 Calibration

Only κ_s is fitted. The calibration condition is the smooth-surface case with $V = 20$ μL and $h = 20$ mm, for which Equation (19) gives $We = 18.32$. A target $\beta^* = 2.25$ was read approximately from Fig. 6(c) of Yilbas et al. [11]; it is a graphical extraction, not a tabulated raw datum. The source article reports an overall experimental uncertainty estimate of approximately 3%, but no additional numerical precision is assigned to the present plot reading.

For the smooth model ($F_{\mathrm{pin}} = 0$, $\phi = 0$), the scalar objective was

$$J(\kappa_s) = \left[\beta_{\max}^{\mathrm{ROM}}(\kappa_s) - \beta^*\right]^2. \tag{21}$$

A bounded one-dimensional root search over $0.1 \le \kappa_s \le 20$ gives $\kappa_s = 6.061$ when the graphical target is matched exactly. The rounded value $\kappa_s = 6.0$ is retained throughout, for which $\beta_{\max}^{\mathrm{ROM}} = 2.252853$. The signed residual is $+0.002853$, or 0.13% of the target. This residual quantifies agreement with the selected calibration value only; it is not an independent validation error.

3.4 Integration, events, and outputs

Equation (3) is integrated with the adaptive RK45 implementation in SciPy [15]. Dense output and bracketed scalar root finding are used to locate velocity reversals, radial return, and crossings of the speed band in Equation (10). The first reported endpoint is the earlier of: (i) the moving-to-stuck event t_s, or (ii) the first retracting crossing $q = q_0$. All plotted trajectories terminate at that endpoint.

For an unpinned trajectory, $\beta_{\max}$ is evaluated at the first positive-to-negative zero of $\dot{q}$. If Equation (10) occurs first during outward motion, $q(t_s)/q_0$ is the reported maximum within the numerical capture band. A radial recovery proxy is defined as

$$e_r^{\mathrm{ROM}} = \begin{cases} |\dot{q}(t_r)|/v_i, & q(t_r) = q_0 \text{ on retraction,} \\ 0, & \text{if the stuck event occurs first.} \end{cases} \tag{22}$$

The value zero in the stuck case is imposed by this definition. The quantity is not the experimental normal restitution coefficient, because the model has no vertical center-of-mass velocity.

3.5 Input reconstruction consistency check

For the 20 μL, 20-mm condition, the reconstructed $We = 18.32$ differs by about 0.7% from the plotted value $We = 18.2$ in Ref. [11]. For the 10, 20, and 30 μL volume sweep at 20 mm, the reconstructed values are 14.54, 18.32, and 20.97, compared with plotted values of approximately 14.4, 18.2, and 20.8. This check concerns input reconstruction only and is independent of the ODE response.

4 Results

4.1 Model hierarchy and base case

Figure 1 and Table 2 compare three models at the calibration condition. The linear unpinned oscillator substantially overpredicts the selected spread target. Cubic stiffening reduces maximum spread from 3.955 to 2.253, demonstrating that the nonlinear restoring term is necessary for the chosen radial representation. Adding textured-surface damping and pinning reduces the predicted maximum further to 1.810. In this hierarchy, the cubic term controls large-deformation stiffness,

while the pinning term supplies additional outward work loss and the hybrid rule determines whether radial retraction continues.

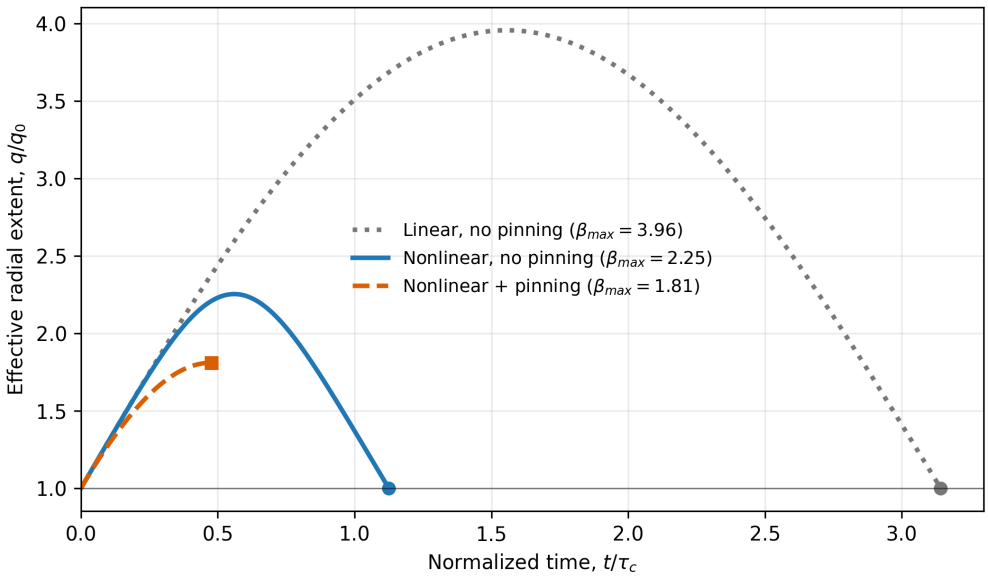


Figure 1: Model hierarchy for $V = 20$ μL and $h = 20$ mm. Each curve ends at its first defined radial endpoint: the first retracting return to $q = q_0$ for the unpinned models or the moving-to-stuck event for the pinned model. Squares mark stuck events and circles mark radial-return events. No unconstrained continuation is displayed.

Table 2: Base-case model hierarchy. The radial recovery proxy is defined by Equation (22).

Model	$\beta_{\max}$	Endpoint (ms)	e_r^{ROM}
Linear, unpinned	3.955	25.561	0.953
Nonlinear, unpinned	2.253	9.152	0.978
Nonlinear, textured/pinned	1.810	3.875	0 (defined)

All three trajectories begin with the same generalized kinetic energy. In the linear model, the potential energy grows only quadratically with deformation, so a comparatively large displacement, $x_{\max} = \beta_{\max} - 1 = 2.955$, is required to arrest the outward motion. The nonlinear model adds a quartic potential contribution and a cubic restoring force; these terms become dominant as x grows and reduce the smooth-surface deformation to $x_{\max} = 1.253$. The earlier reversal is therefore a direct consequence of amplitude-dependent stiffness rather than increased damping. This comparison explains why fitting the large-deformation response with a linear spring would require an unrealistically large constant stiffness and would lose the correct inertial–capillary timescale near the reference state.

For the textured case, work is additionally removed during outward motion by the regularized pinning term. The trajectory reaches the moving-to-stuck capture band at $x = 0.810$, before the unpinned nonlinear oscillator reaches its turning amplitude. Thus the modeled 19.7% reduction from the nonlinear smooth value to the textured value is produced by the combined effects of outward pinning work and the hybrid static-capacity rule. Its direction agrees with the experimental trend reported by Yilbas et al. [11], but the comparison is not an independent pointwise validation: the

smooth base point was used for calibration, while the textured response depends on the assumed pinning closure. The endpoint times in Table 2 also represent different radial events and must not be interpreted as comparative physical contact times.

4.2 Fixed-parameter condition transfer

After calibration, κ_s, ζ_0, v_s, v_{stick}, and η_s are held fixed. Quantities that depend on volume or release height are recomputed. Table 3 and Figure 2 show that the predicted maximum spread increases monotonically with We for both surfaces, while the textured result remains smaller at every investigated condition. These directions agree with the graphical trends in Ref. [11]; numerical pointwise errors are not reported because a tabulated experimental response dataset was not used.

Table 3: Model-only condition transfer with closure parameters fixed.

V (μL)	h (mm)	We	$\beta_{\max}$ smooth	$\beta_{\max}$ textured
20	10	9.16	2.030	1.474
10	20	14.54	2.174	1.688
20	20	18.32	2.253	1.810
30	20	20.97	2.301	1.884
20	30	27.48	2.400	2.034

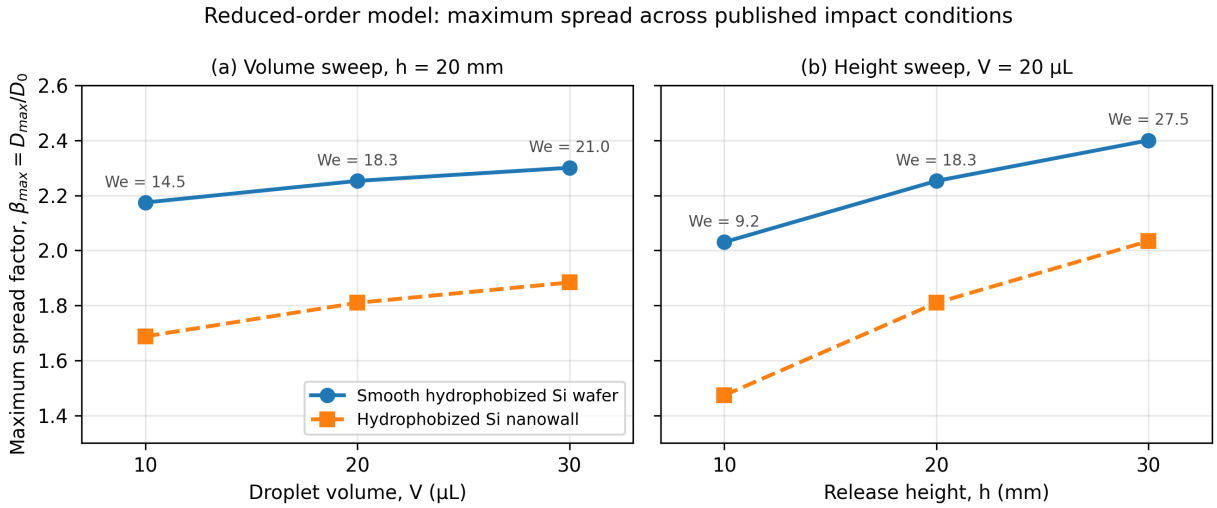


Figure 2: Fixed-parameter maximum-spread predictions for (a) the droplet-volume sweep at $h = 20$ mm and (b) the release-height sweep at $V = 20$ μL. Reconstructed Weber numbers are annotated above the smooth-surface points. Lines connect discrete model evaluations and are not continuous experimental fits.

The two panels also separate the effects of the reconstructed input variables. With ballistic impact speed and spherical-equivalent diameter, $We \propto hV^{1/3}$. A threefold change in release height therefore changes We threefold, whereas a threefold change in volume changes it only by $3^{1/3}$. This explains why the height sweep spans $We = 9.16$–27.48 and produces a larger spread variation than the volume sweep, which spans $We = 14.54$–20.97. The difference is a consequence of the reconstructed dimensionless forcing, not evidence that height is itself an independent material control.

The dimensionless initial radial speed provides a more direct interpretation:

$$x'(0) = \frac{v_i \tau_c}{q_0} = \sqrt{\frac{We}{2}}. \tag{23}$$

Under the adopted $D_H = 2a$ closure, Π_{pin} is constant, while $x'(0)$ increases with We. Increasing impact severity therefore raises the initial inertial drive relative to the dimensionless pinning barrier. Consistently, the modeled relative spread reduction decreases from 27.4% to 15.3% across the height sweep and from 22.4% to 18.1% across the volume sweep. The textured and smooth curves approach one another in relative terms but do not cross in the investigated range. This is a mechanistic consequence of the present nondimensional structure; it does not establish that the experimental texture force is truly independent of spacing, deformation, or contact-line radius.

4.3 Local deterministic sensitivity

Figure 3 restores the full one-factor-at-a-time response map for the four continuous closure parameters. Both surfaces are shown because a parameter can have different roles in the unpinned and pinned systems. These calculations diagnose local deterministic dependence over ±25% about the base case; they are not uncertainty quantification and do not assign probability distributions to the inputs.

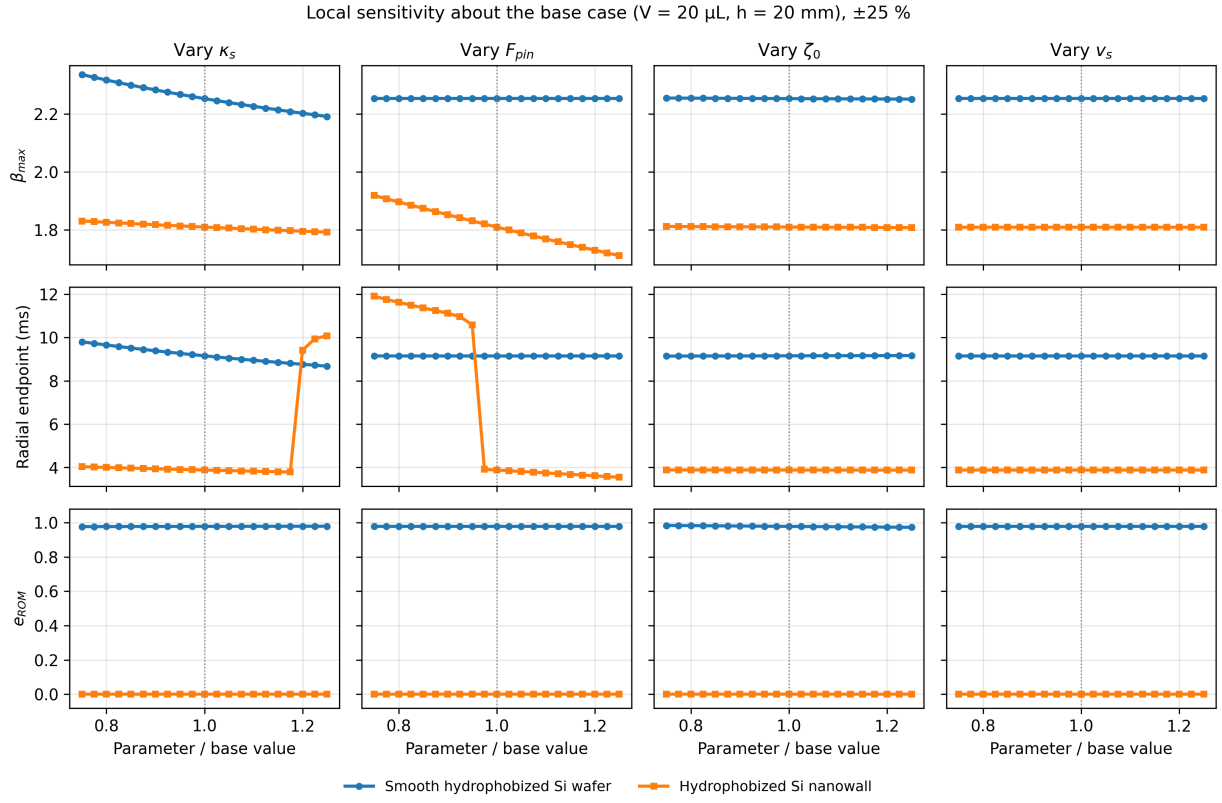


Figure 3: Local deterministic sensitivity about the base case. Columns vary κ_s, F_{pin}, ζ_0, and v_s over 0.75–1.25 times their base values; dotted vertical lines mark the base case. Rows show maximum spread, first radial endpoint time, and the radial recovery proxy. Abrupt endpoint changes are switches between immediate and delayed stuck-event branches, not numerical discontinuities in $\beta_{\max}$.

The upper row isolates the maximum-spread controls. Increasing κ_s reduces $\beta_{\max}$ on both surfaces because the cubic restoring force grows as x^3. Over the plotted interval, the smooth result decreases from 2.336 to 2.191, whereas the textured result decreases only from 1.831 to 1.792. The weaker textured sensitivity occurs because pinning has already limited the deformation before the quartic potential becomes as influential as it is on the smooth trajectory. In contrast, changing F_{pin} leaves the smooth solution identically unchanged but moves the textured prediction from 1.918 to 1.711. Pinning magnitude is therefore the dominant texture-specific control in this local range.

The damping and regularization columns have different interpretations. A $\pm 25\%$ change in ζ_0 changes the textured $\beta_{\max}$ only from 1.812 to 1.808 and the smooth value only from 2.255 to 2.251. This weak response is consistent with the low-Oh, high-Re base condition and with the scaling $\zeta \propto Re^{-1/2}$. Varying v_s produces no visible change because v_s affects only a narrow velocity interval near reversal; it does not set the magnitude of the resistance during most of the outward motion. The near invariance to v_s is a useful numerical check, whereas the response to F_{pin} is a structural model dependence.

The middle row reveals information that is hidden by a plot of $\beta_{\max}$ alone. At $\kappa_s/\kappa_{s,0} \approx 1.20$, the textured endpoint jumps from approximately 3.8 ms to more than 9 ms. A complementary jump occurs between $F_{\mathrm{pin}}/F_{\mathrm{pin},0} = 0.95$ and 0.975. On one side of these thresholds, the static capacity is sufficient to arrest the coordinate at the first outward turning region; on the other, the coordinate retracts and is arrested only at a later low-speed encounter. Maximum spread remains smooth across the switch because it is set during the first outward excursion, but endpoint time changes discontinuously because it identifies a different hybrid event branch. Endpoint time is therefore intrinsically ill-conditioned near this boundary and is unsuitable as a smooth calibration objective.

The bottom row should be read only as a radial state diagnostic. The smooth trajectory returns to q_0 throughout the sweep and has $e_r^{\mathrm{ROM}} \simeq 0.98$. Every textured trajectory shown reaches a stuck event first, so its proxy is zero by definition. The flat zero curves do not imply zero experimental rebound and do not demonstrate insensitivity of vertical restitution to the varied parameters.

Table 4 complements the continuous response map with checks on the static-capacity factor, sticking-speed band, event tolerance, and solver settings. The maximum spread is essentially unchanged by these numerical/event choices at the reported precision. Endpoint classification is less robust: reducing η_s to 0.9 removes the detected stuck or return event within $5\tau_c$, illustrating that the hybrid state boundary is a modeling assumption even when the moving trajectory and its maximum are stable.

Table 4: Sensitivity and reproducibility checks for the textured base case. "No event" means neither stuck nor $q = q_0$ return was found within $5\tau_c$.

Quantity varied	Levels	$\beta_{\max}$ range	Endpoint range (ms)	Main observation
κ_s	4.5, 6.0, 7.5	1.831–1.792	3.875–10.078	Stiffening lowers spread; event branch changes
$F_{\mathrm{pin}}/F_{\mathrm{pin},0}$	0.75, 1, 1.25	1.918–1.711	3.540–11.900	Dominant textured spread control
η_s	0.9, 1.0, 1.1	1.810–1.810	no event–3.875	Static threshold controls event existence
v_{stick} ($\mathrm{m\,s^{-1}}$)	10^{-4}–10^{-2}	1.810–1.810	3.833–3.879	Small capture-band influence
v_s ($\mathrm{m\,s^{-1}}$)	10^{-5}–10^{-3}	1.810–1.810	3.875–3.875	Negligible at shown precision
Event tolerance (s)	10^{-8}–10^{-12}	1.810–1.810	3.875–3.875	Negligible at shown precision
Solver settings	coarse–fine	1.810–1.810	3.875–3.875	Numerically reproducible

For the solver check, the coarse case uses rtol 10^{-5}, atol 10^{-9}, and $\Delta t_{\max} = \tau_c/12.5$; the fine case uses rtol 10^{-8}, atol 10^{-12}, and $\Delta t_{\max} = \tau_c/50$. The maximum variation across these cases is

below 10^{-6} in $\beta_{\max}$ and below 10^{-3} ms in the endpoint time. Numerical refinement is therefore much smaller than the structural dependence on the pinning closure.

4.4 Radial recovery proxy

The nonlinear unpinned model gives $e_r^{\mathrm{ROM}} = 0.978$. The textured base case reaches the stuck event before returning to q_0, so Equation (22) assigns $e_r^{\mathrm{ROM}} = 0$. This zero is a classification convention for radial non-return. It is neither a prediction of zero rebound height nor a normal restitution coefficient. Consequently, it must not be compared numerically with the vertical restitution data in Ref. [11]. The proxy is retained only to document whether the modeled radial coordinate recovers its reference value before the imposed stuck event.

5 Limitations and Implications

The model's defensible output is the first maximum of an effective radial coordinate. It does not resolve the liquid–gas interface, internal circulation, pressure, lamella or rim geometry, gas cushioning, penetration into texture, or local contact-line motion. It also omits advancing/receding contact-angle hysteresis, although such physics is important for pinned droplet oscillations [5, 6]. Cassie-like and penetrated configurations are not separate model states; Wenzel or Cassie–Baxter terminology is therefore used only as physical context, not as a predicted transition.

The hybrid stuck rule corrects a mathematical inconsistency in attributing static pinning to a smooth odd force that vanishes at zero speed. Nevertheless, Equation (10) remains an imposed closure. Near its switching boundary, small changes in η_s, F_{pin}, or κ_s can cause large changes in endpoint time even when $\beta_{\max}$ varies smoothly. The endpoint is therefore a state-classification diagnostic, not a prediction of physical contact time. A pinned radial coordinate could remain in liquid–solid contact, later depin, or participate in vertical motion, none of which is represented.

The energy balance in Equation (18) contains only losses beyond the conservative radial spring. It cannot represent recoverable energy stored in a gas pocket or texture-scale interface, and the single coordinate cannot determine how energy is redirected into vertical center-of-mass motion. The model therefore makes no claim about trapped-air spring-back, rebound height, vertical momentum, physical lift-off, or normal restitution. A model for those outputs would require at least a vertical coordinate and a contact-state rule; a resolved multiphase treatment would additionally be needed for detailed interface, pressure, gas, and wetting-state fields [8].

There is also no unilateral constraint $q \geq 0$. If the nonlinear smooth oscillator is continued beyond the reported first radial-return event, it reaches $q = 0$ at approximately $t/\tau_c = 1.49$ and then becomes negative. This behavior is not a physical droplet prediction or a solver instability; it demonstrates that a signed radial oscillator is invalid after the defined first-cycle event. All figures and reported quantities terminate before that unphysical continuation.

Within these limits, the hierarchy provides a reproducible interpretation of maximum spread. The linear oscillator is too compliant for the selected base condition; nonlinear stiffness brings the smooth result to the calibration target; and the assumed textured-surface resistance produces a lower maximum spread and the correct qualitative ordering across reconstructed conditions. The results identify which conclusions follow from the calculation and which depend on closures requiring future experimental or resolved-simulation support.

6 Conclusions

A nonlinear one-degree-of-freedom radial model was reformulated for transparent use as an arXiv preprint. The state is an effective radial extent, and the whole-droplet mass and impact-to-radial velocity mapping are explicit lumped assumptions. Static pinning is implemented by a stated moving-to-stuck rule rather than attributed to the regularized kinetic force at zero speed. The pinning estimate is a fixed-reference closure; with $D_H = 2a$, its dimensionless magnitude is independent of texture spacing, which is a clear limitation.

At the 20 μL, 20-mm calibration condition, the linear, nonlinear-unpinned, and nonlinear-pinned models give $\beta_{\max} = 3.955$, 2.253, and 1.810, respectively. With fixed parameters, maximum spread increases with reconstructed Weber number and remains lower for the textured surface over the investigated conditions. These are qualitative and cross-condition model trends, not definitive experimental validation. Local deterministic sensitivity identifies nonlinear stiffness and pinning magnitude as the main controls, while the numerical integration and event localization are reproducible at the reported precision.

The model cannot predict vertical rebound, normal restitution, physical contact time, lift-off, wetting-state transitions, trapped-air dynamics, or detailed multiphase fields. Its useful scope is a reproducible first-maximum radial surrogate and an explicit baseline for future two-coordinate or resolved models.

Acknowledgments

The authors acknowledge the Department of Mechanical Engineering, Ahmadu Bello University (ABU), Zaria.

References

[1] Clanet, C.; Béguin, C.; Richard, D.; Quéré, D. "Maximal Deformation of an Impacting Drop." *J. Fluid Mech.* **2004**, 517, 199–208. https://doi.org/10.1017/S0022112004000904

[2] Roisman, I.V. "Inertia Dominated Drop Collisions. II. An Analytical Solution of the Navier–Stokes Equations for a Spreading Viscous Film." *Phys. Fluids* **2009**, 21, 052104. https://doi.org/10.1063/1.3129283

[3] Wenzel, R.N. "Resistance of Solid Surfaces to Wetting by Water." *Ind. Eng. Chem.* **1936**, 28, 988–994. https://doi.org/10.1021/ie50320a024

[4] Cassie, A.B.D.; Baxter, S. "Wettability of Porous Surfaces." *Trans. Faraday Soc.* **1944**, 40, 546–551. https://doi.org/10.1039/TF9444000546

[5] Joanny, J.F.; de Gennes, P.G. "A Model for Contact Angle Hysteresis." *J. Chem. Phys.* **1984**, 81, 552–562. https://doi.org/10.1063/1.447337

[6] Dwivedi, R.K.; Jain, V.; Muralidhar, K. "Dynamic Contact Angle Model for Resolving Low-Viscosity Droplet Oscillations during Spreading over a Surface with Varying Wettability." *Phys. Rev. Fluids* **2022**, 7, 034002. https://doi.org/10.1103/PhysRevFluids.7.034002

[7] Bartolo, D.; Bouamrirene, F.; Verneuil, E.; Buguin, A.; Silberzan, P.; Moulinet, S. "Bouncing or Sticky Droplets: Impalement Transitions on Superhydrophobic Micropatterned Surfaces." *Europhys. Lett.* **2006**, 74, 299–305. https://doi.org/10.1209/epl/i2005-10522-3

[8] Xia, L.; Chen, F.; Liu, T.; Zhang, D.; Tian, Y.; Zhang, D. "Phase-Field Simulations of Droplet Impact on Superhydrophobic Surfaces." *Int. J. Mech. Sci.* **2023**, 240, 107957. https://doi.org/10.1016/j.ijmecsci.2022.107957

[9] Yakubu, M. "Dynamics of Water Droplet Spinning and Rolling on Inclined Superhydrophobic Wedge Channel." Master's thesis, King Fahd University of Petroleum and Minerals, Dhahran, Saudi Arabia, 2020. https://eprints.kfupm.edu.sa/id/eprint/141657/

[10] Yakubu, M.; Yilbas, B.S.; Abubakr, A.A.; Al-Qahtani, H. "Droplet Rolling and Spinning in V-Shaped Hydrophobic Surfaces for Environmental Dust Mitigation." *Molecules* **2020**, 25, 3039. https://doi.org/10.3390/molecules25133039

[11] Yilbas, B.S.; Abubakar, A.; Yakubu, M.; Al-Qahtani, H.; Al-Sharafi, A. "Nanowall Textured Hydrophobic Surfaces and Liquid Droplet Impact." *Materials* **2022**, 15, 1645. https://doi.org/10.3390/ma15051645

[12] Abubakar, A.A.; Yilbas, B.S.; Yakubu, M.; Al-Qahtani, H.; Hassan, G.; Adukwu, J.E. "Impacting Droplet Can Mitigate Dust from PDMS Micro-Post Array Surfaces." *Coatings* **2021**, 11, 1377. https://doi.org/10.3390/coatings11111377

[13] Okumura, K.; Chevy, F.; Richard, D.; Quéré, D.; Clanet, C. "Water Spring: A Model for Bouncing Drops." *Europhys. Lett.* **2003**, 62, 237–243. https://doi.org/10.1209/epl/i2003-00340-1

[14] Biance, A.-L.; Clanet, C.; Quéré, D. "First Steps in the Spreading of a Liquid Droplet." *Phys. Rev. E* **2004**, 69, 016301. https://doi.org/10.1103/PhysRevE.69.016301

[15] Virtanen, P.; Gommers, R.; Oliphant, T.E.; et al. "SciPy 1.0: Fundamental Algorithms for Scientific Computing in Python." *Nat. Methods* **2020**, 17, 261–272. https://doi.org/10.1038/s41592-019-0686-2